

Particlization in hybrid models

Pasi Huovinen¹ and Hannah Petersen²

¹ Institut für Theoretische Physik, Johann Wolfgang Goethe-Universität, D-60438 Frankfurt am Main, Germany

² Department of Physics, Duke University, Durham, NC 27708-0305, USA

Abstract. In hybrid models, which combine hydrodynamical and transport approaches to describe different stages of heavy-ion collisions, conversion of fluid to individual particles, particlization, is a non-trivial technical problem. We describe in detail how to find the particlization hypersurface in a 3+1 dimensional model, and how to sample the particle distributions evaluated using the Cooper-Frye procedure to create an ensemble of particles as an initial state for the transport stage. We also discuss the role and magnitude of the negative contributions in the Cooper-Frye procedure.

PACS. 24.10.Lx Monte Carlo simulations – 24.10.Nz Hydrodynamic models

1 Introduction

In recent years the so-called hybrid models [1, 2, 3, 4, 5, 6, 7, 8, 9] have become very popular in describing the expansion and evolution of the hot dense matter created in ultrarelativistic heavy-ion collisions. In these models the different stages of the expansion are described using different models: The early stages of the expansion, when the matter is presumably partonic, are described using ideal or dissipative fluid dynamics, whereas the late dilute stage after hadronization is described using a hadronic transport model like RQMD [10], UrQMD [11] or JAM [12].

Hybrid models are conceptually attractive since they attempt to combine the best features of fluid dynamics and transport: The complicated microscopic dynamics of hadronization can be sidestepped by assuming it to happen adiabatically, in which case it can be described using fluid dynamics. On the other hand, the dilute hadronic matter is assumed to be highly dissipative and deviate gradually from local equilibrium. Description of such a matter using fluid dynamics is demanding, but is trivial using microscopic transport, which by construction can handle matter arbitrarily far from equilibrium. Also, the transport models describe the last rescattering of particles, so-called freeze-out, based on individual scattering cross sections. Thus freeze-out is not controlled by a parameter which value is known only after comparison with data.

Furthermore, it has been realised that a consistent comparison with the data is easier if one generates an ensemble of particles event-by-event, and analyses these ensembles in a similar way than the actual data has been analysed [9, 13, 14]. In hybrid models this requires no further effort since the transport models are based on propagation of individual particles along their semiclassical tra-

jectories, and thus require the generation of such ensembles to begin with.

However, connecting two approaches with very different degrees of freedom — densities, velocity, and possible dissipative currents in the fluid, and individual particles in the cascade — is highly nontrivial. Instead of running hydro and cascade side by side and using the cascade calculation to provide the boundary conditions for fluid dynamics, all the present hybrid models solve fluid dynamics independently of the cascade taking the boundary condition as vacuum at infinity (see discussion in Ref. [15]). The boundary where one switches from fluid dynamical to transport description is then determined a posteriori, once the evolution of the fluid is known. This boundary, or switching surface, is usually chosen to be a surface of constant temperature, energy density, or time. The particle distributions on this surface are evaluated using the Cooper-Frye procedure [16]. These distributions are sampled to generate an ensemble of particles with well defined positions and momenta, and these ensembles are used as an initial state for the transport stage. Note that even if the transport stage describes the final freeze-out of the particles without additional parameters, the choice of the criterion where to switch from fluid to cascade is an equally free parameter than the freeze-out temperature in a conventional hydrodynamical model. Unfortunately the final results are also somewhat sensitive to this switching criterion as discussed in Ref. [9], and as we will discuss later.

We want to emphasise that this switching from fluid dynamics to transport is not freeze-out. By definition, there are no rescatterings, only resonance decays after freeze-out. Thus, if one switches from fluid to transport at freeze-out, the transport stage is unnecessary. It does nothing else but lets the resonances decay. On the other hand, the switching is not necessarily hadronization either.

Since the deconfinement transition is a smooth crossover, there is no clear point where hadronization should take place, and it is easier to choose to switch at a stage where the system has already hadronized. In the following we assume that there is no change in the physics nor in the properties of the system on the switching surface. It is only a change in the description of the system. Thus we call the process of changing from fluid dynamics to transport particlization, conversion of fluid to particles.

In this paper we describe some technical aspects of particlization in hybrid models, and how different choices of the switching criterion and constraints imposed to the sampling of the distributions affect the final particle distributions in $E_{\text{lab}} = 160A$ GeV Pb+Pb (SPS) and $\sqrt{s_{\text{NN}}} = 200$ GeV Au+Au (RHIC) collisions. In particular we discuss finding the particlization surface and its properties in section 2, the negative contributions of Cooper-Frye procedure and how to take them into account when sampling the distributions in section 3, the actual sampling procedure in section 4, and calculations within one specific hybrid approach in section 5.

2 Surface finding

The Cooper-Frye procedure [16] for calculating particle distributions on a surface is based on evaluating a particle four-current through a surface, and a kinetic theory decomposition of a four-current j^μ in terms of particle distribution $f(p, x)$:

$$N = \int_{\sigma} d\sigma_{\mu} j^{\mu}(x) = \int_{\sigma} d\sigma_{\mu} \int \frac{d^3p}{E} p^{\mu} f(x, p) \\ \implies E \frac{dN}{dp^3} = \int_{\sigma} d\sigma_{\mu} p^{\mu} f(x, p) \approx \sum_{\sigma} \Delta\sigma_{\mu} p^{\mu} f(x, p). \quad (1)$$

Thus one needs to find not only the location of the surface σ where one applies the Cooper-Frye formula, but also its normal. If we knew the analytic expression for the surface, its normal would be simply given by [17,18]

$$d\sigma_{\mu} = \varepsilon_{\mu\alpha\beta\gamma} \frac{\partial x^{\alpha}}{\partial a} \frac{\partial x^{\beta}}{\partial b} \frac{\partial x^{\gamma}}{\partial c} da db dc, \quad (2)$$

where a, b, c are the coordinates on the surface and $\varepsilon_{\mu\alpha\beta\gamma}$ is the totally antisymmetric Levi-Civita tensor. However, we do not have an analytic expression since we solve the evolution of the system numerically. Finding the location of an isosurface on a discrete grid is easy, but evaluating the size¹ and normal of each discrete surface element is not, since one has to make sure that the surface elements cover the entire surface without leaving holes or double counting any part of the surface.

In computer graphics and image processing the problem of finding an isosurface of a discrete scalar field is well known, and many algorithms have been proposed for the task, see, *e.g.* Ref. [19], and references therein. One

of the best known of these algorithms is so called Marching Cubes algorithm [20], a simplified version of which was implemented in a hydrodynamical model by Kataja and Venugopalan [21], and subsequently used in AZHYDRO [22]. The original Marching Cubes algorithm was extended for hypersurfaces in four dimensional space in Ref. [19], and a simplified version implemented in a 3+1 dimensional hydrodynamical model by Schenke [23]. However, it is known that the original Marching Cubes algorithm cannot resolve all possible surface configurations, and may leave holes in the final surface [24,25]. This problem is not serious: As quoted in Ref. [23], only 1% of the surface elements in a typical heavy-ion collision calculation are not fully resolved. But, if one is doing event-by-event hydrodynamical calculations with irregular initial conditions, one may expect much more complicated structures to appear, and the Marching Cubes algorithm may leave more holes in the surface. To avoid this problem altogether, we have slightly modified the algorithm proposed in Ref. [26], and generalised it for finding a three dimensional hypersurface in four dimensional space². For the lack of a better name, we call it here “disordered lines” algorithm. This algorithm may also have been implemented in Ref. [17], but the description there is too vague to tell.

In algorithms solving the equations of motion of fluid dynamics like SHASTA [27], a grid point is considered to be in the middle of a corresponding volume element. For purposes of surface finding it is useful to consider the dual of the grid, where the grid points are thought to be at the corners of a volume element, and the values within a volume element can be obtained by interpolation. To find the location of the surface it is practical to “march” through the entire grid and check every volume element whether the values at the corners are all above or all below the isovalue. If not, *i.e.* if some of the corners are above, and some below the isovalue, the surface passes through this volume element.

An alternative to this exhaustive search method is the continuation method [28], which after finding a surface element, checks only the neighbouring volume elements which one of them contains the surface, moves to that element, and continues until it either finds the edge of the grid or returns to the volume element it found first. The continuation method is faster than the exhaustive search, but if the surface is disjoint, it will not necessarily find all parts of the surface, whereas the exhaustive search method by construction finds all parts of the surface.

In the following we call volume elements (hyper)cubes, and explain the algorithm in a 3D case first. Once a cube containing the isosurface is found, the positions of the isosurface on the edges of the cube can be found by linear interpolation, see illustration in Fig. 1. How to sort these intersection points to form a polygon (or a polyhedron in 4D) which does not cross itself is the crucial part of any algorithm. It can be done in three different ways [29]: By using protomeshes [30], by using a lookup table like

¹ The size enters as the length of the discrete normal vector $\Delta\sigma_{\mu}$.

² Fortran and C++ subroutines, cornelius, implementing this algorithm in 3D and 4D, are available at <https://karman.physics.purdue.edu/OSCAR/>

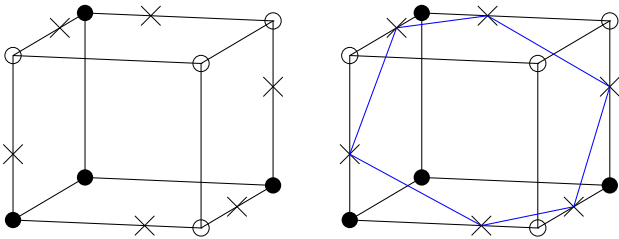


Fig. 1. A 3D volume element, a cube, with four corners above (solid dots) and four below (open dots) the isovalue. In the left panel the points where the interpolated value is the isovalue are marked with crosses. In the right panel these intersection points have been connected to form a polygon. This polygon is a surface element of the isosurface.

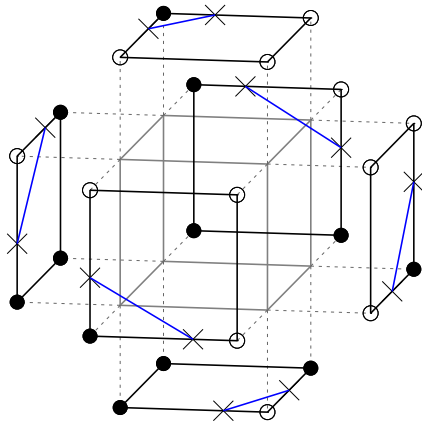


Fig. 2. Reduction of a three dimensional problem into a series of two dimensional problems: We find the surface element by looking for its edges on the faces of the cube.

in the original Marching Cubes algorithm [19,20,25], or algorithmically [28,31,32,33] like we do here.

In three or more dimensions the ordering of the intersection points is difficult because of the many possibilities involved, but in two dimensions it is almost trivial. Therefore we reduce the problem of finding the surface into a series of two dimensional problems of finding a line within a square, a line which is an edge of the polygon we want to find, see Figs. 1 and 2. If all of the corners of a square are above or below the isovalue, there is of course no edge of the polygon there. If only one of the corners is above or below, we have the configuration shown in Fig. 3 a), and if two neighbouring corners are above the isovalue, the configuration is shown in Fig. 3 b). The case where two corners above the isovalue are located diagonally is ambiguous. How to choose between configurations shown in Figs. 3 c) and d)? We follow the original idea of Ref. [26]: If the value interpolated at the center of the square is above or equal to the isovalue, the center must be inside of the surface, and if it is below, the center must be outside of

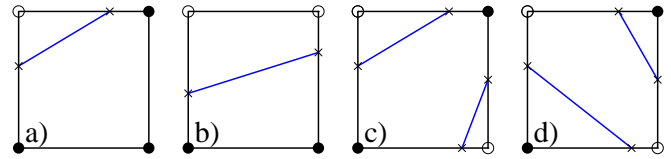


Fig. 3. The nontrivial cases of connecting intersection points at the edges of the face.

the surface. A more sophisticated rule has been suggested in Refs. [25,31]: The values on the face are interpolated bilinearly. The isocontours in a bilinear interpolation are hyperbolas, and thus one should interpolate the value at the center of this hyperbola to decide whether the corners above or below the isovalue are linked. A special case occurs when the value in any of the cube corners is the isovalue. In that case we consider such a corner to be within the surface, and place intersection points 10^{-9} times the edglength away from the corner, on those edges of the cube where the neighbouring corner has a value smaller than the isovalue.

After the intersection points at each face have been found, each edge of the polygon is characterised by two points: its ends. An important difference between our algorithm and that of Refs. [26,31] is that in most common cases we do not need to order the edges of the polygon so that the next edge in the list begins where the previous one ends. We may check the faces of the cube in arbitrary order, and keep the edges of the polygon stored in the same arbitrary order. Important exceptions to this rule are the cases where the face by face search returns six or more edges: The surface may consists of two or more disconnected parts, see Fig. 4, and we have to sort the edges in sequence to find out whether the surface is disjoint, and which edges belong to which polygon. We group the edges accordingly, and treat the separate polygons independently of each other.

Note that allowing the surface to consist of several parts is necessary for the consistency of the surface. Fig. 4 depicts a case when a badly resolved ambiguity on a face may lead to a hole on the surface, or counting parts of the surface twice. Since we solve the ambiguities by using only the information available at the face of a cube, the face is always resolved in the same way, no matter in which cube it is taken to belong to. Thus the surface elements form a consistent surface without holes nor double counted elements. Furthermore, the rules we described are sufficient to resolve any configuration of values at the cube corners.

After the possible ordering of the edges and dividing them in separate groups if they form two or more disconnected surface elements, we evaluate the area and normal of the polygon(s). The use of Cooper-Frye procedure requires not only the surface area and normal, but also the values of the hydrodynamical fields on the surface. They are best evaluated as interpolated values at the centroid of the surface. Since we have to evaluate the centroid for this purpose anyway, we triangularise the polygon using the centroid: By connecting the ends of each edge of the polygon to the centroid, we obtain a set of triangles which

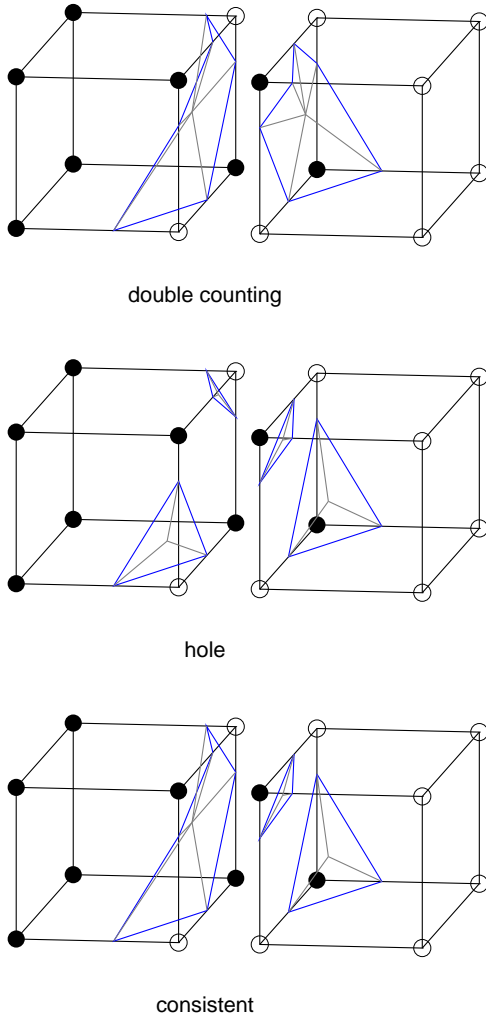


Fig. 4. An example of a configuration where badly resolved ambiguity may lead to double counting or a hole on the surface. The cubes left and right represent neighbouring cubes separated for the sake of clarity.

cover the entire polygon. As depicted in Fig. 5, the polygon is not necessarily planar. A sum of the areas and normal vectors of the triangles approximates the area and normal of the polygon as

$$\Delta\sigma = \sum_i \frac{1}{2} f_i \mathbf{a}_i \times \mathbf{b}_i, \quad (3)$$

where \mathbf{a}_i and \mathbf{b}_i are vectors from the centroid to the ends of the i th edge of the polygon, and $f_i = \pm 1$ is chosen so that each of the normal vectors $\frac{1}{2} f_i \mathbf{a}_i \times \mathbf{b}_i$ is directed towards lower values, *i.e.* outside.

To make the illustrations of the hypersurfaces in a hypercube more understandable, we first show a simple 2D projection of a 4D hypercube in Fig. 6, and how an evolving 2D surface in 3D space spans a 3D hypersurface in 4D spacetime in Fig. 7. This hypersurface element forms a polyhedron within a hypercube (Fig. 8), and like a poly-

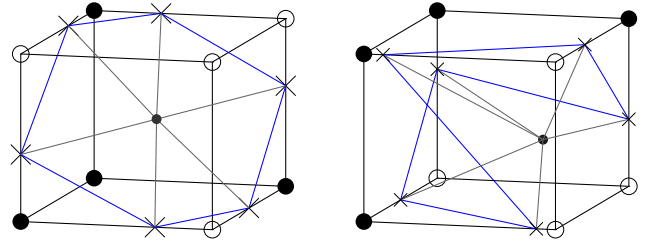


Fig. 5. Examples of triangularisation of the polygon in a simple and a complicated case.

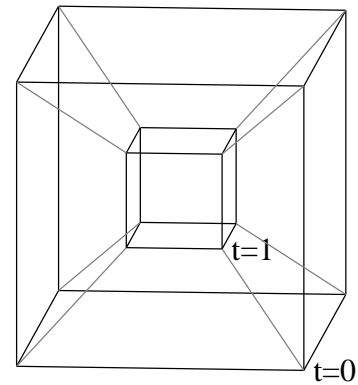


Fig. 6. A 2D projection of a 4D hypercube. In the figure, the cube in the middle is the hyperface of the hypercube at coordinate $t = 1$, the large cube around it is the hyperface at $t = 0$, and the grey lines connecting them are edges with constant values of coordinates x, y, z .

gon can be divided into a group of triangles, a polyhedron can be divided into tetrahedra.

We proceed analogously to the 3D case. We first divide the problem into eight three dimensional problems: As a cube consists of six squares, a hypercube consists of eight cubes, see Fig. 9. The surface in each of these is found in the same way than described above. The centroid of these 2D surfaces, which form the faces of the tetrahedra, is calculated, and the corners of the triangles forming these faces are recorded. This is illustrated in Fig. 8, where the triangularisation of the face within the $t = 0$ hyperface is shown.

As in 3D the ordering of the edges is not important unless the surface consists of several disconnected parts. If the number of edges and the number of hypercube corners above and below isovalue indicate that this is possible, we order the edges to group them according to the polyhedron they belong to, and treat the groups as separate surfaces.

We evaluate an approximative centroid for the polyhedron. Analogously to the 2D surface in a 3D space, connecting the centroid to the corners of the triangles forming the faces of the polyhedron, creates a set of tetrahedra which fills the volume of the polyhedron, see Fig. 10. The

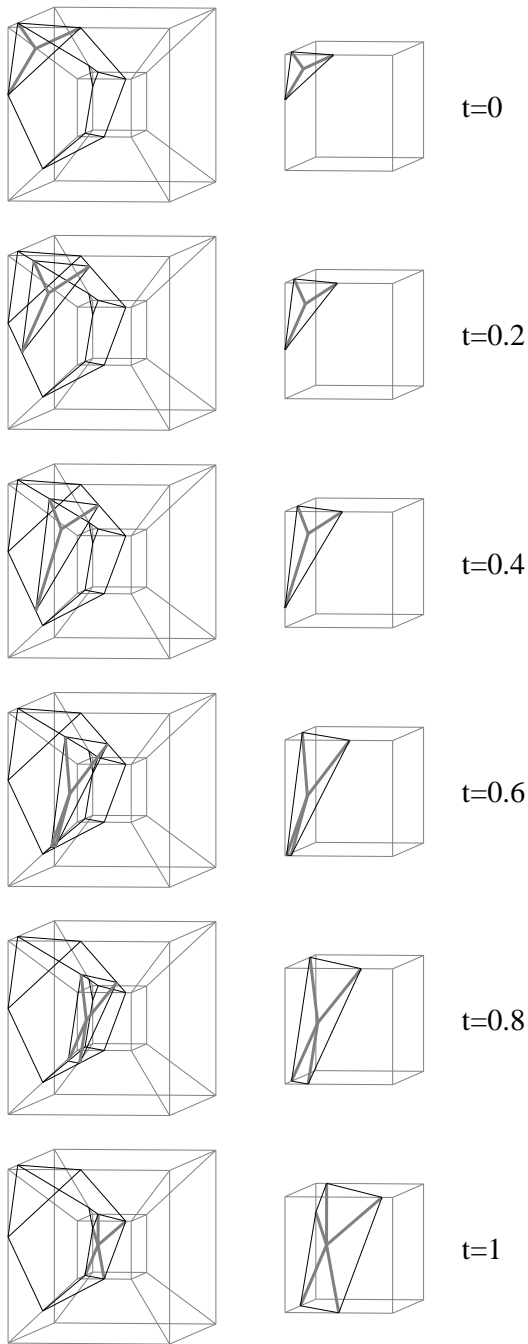


Fig. 7. Time evolution of a surface element in four (left) and three dimensional (right) representation of a volume element. A 2D polygon moving in time spans a 3D polyhedron in a hypercube.

hyperarea, *i.e.* the volume, of the polyhedron and its normal can be calculated as a sum of the volumes and normals of its constituent tetrahedra [23]:

$$\Delta\sigma_\mu = \sum_i \varepsilon_{\mu\alpha\beta\gamma} \frac{1}{6} f_i a_i^\alpha b_i^\beta c_i^\gamma, \quad (4)$$

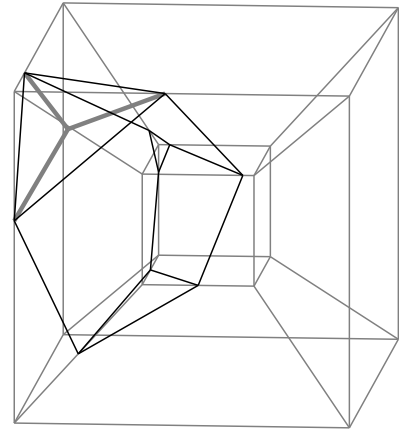


Fig. 8. A hypersurface element, a polyhedron, within a hypercube. A triangularisation of the polyhedron's face with $t = 0$ is shown. We do not show the triangularisation of the other faces for the sake of clarity.

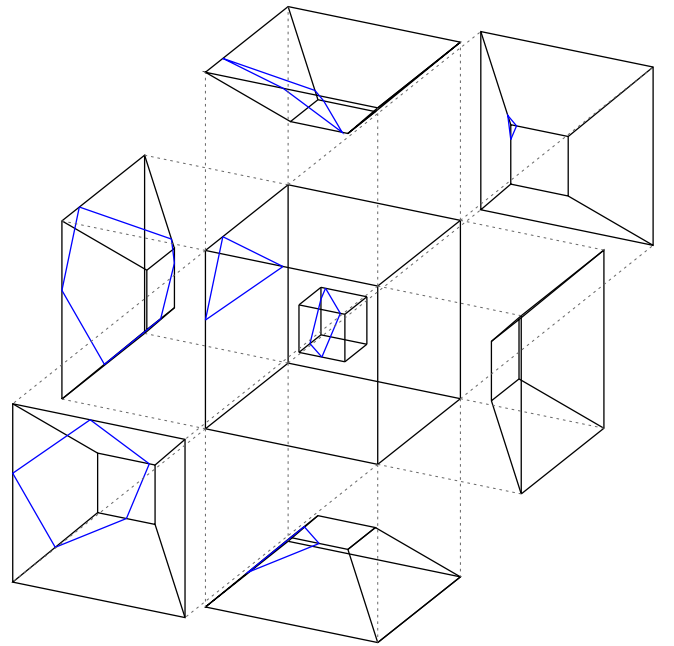


Fig. 9. Reduction of a four dimensional problem into a series of three dimensional problems.

where a_i , b_i and c_i are vectors from the centroid to the corners of the i th triangle, and $f_i = \pm 1$ chosen so that each of the normal vectors of the tetrahedra is directed towards lower values, *i.e.* outside.

We want to emphasise that this algorithm is by no means the only approach for creating consistent surfaces with no holes nor double counting [25,31,32]. Especially Bernd Schlei's VESTA and STEVE algorithms [30], used

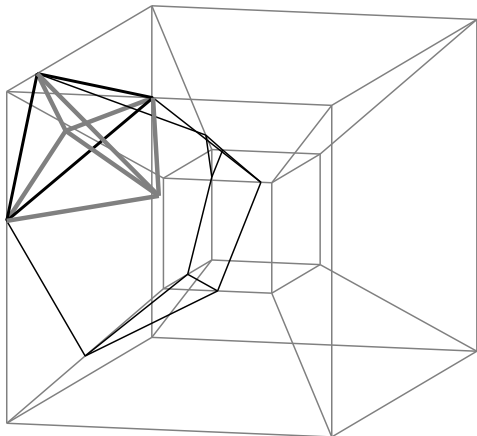


Fig. 10. A part of the tetrahedronisation of the polyhedron based on triangularisation of the faces of the polyhedron. Full tetrahedronisation is not shown for the sake of clarity.

in Ref. [34], are faster than ours and produce even higher quality surfaces.

In the recent heavy-ion physics literature two other algorithms for finding a surface in four dimensions have been described. In Ref. [9] the surface elements are taken to be the common faces of neighbouring volume elements when the isovalue is reached between them. This algorithm is simple and robust, but it requires very small grid spacing to avoid numerical artefacts (see discussion in Refs. [23, 33]). “Very small” in this context means that the volume element for the surface extraction should be the same than the volume element for the fluid evolution, whereas the more sophisticated algorithms discussed here allow significantly larger volume elements for surface evaluation than for fluid evolution. For example, in Ref. [35] the results were calculated using timestep $\Delta\tau = 0.04$ fm and grid spacing $\Delta x = \Delta y = 0.1$ fm, whereas the surface elements were evaluated in cubes 10 times larger in time, and 2 to 4 times larger in both spatial directions (depending on the impact parameter). In the following, however, we play it safe and use the same grid spacing and timestep for both the hydrodynamical evolution and surface extraction to calculate the results shown in Sec. 5.

Another algorithm was described in Ref. [33] and called a projection method. To our understanding this method insists that there is only one surface element within each volume element. As discussed above this may lead to double counting some parts of the surface.

3 Negative contributions of Cooper-Frye

One of the conceptual problems in using the Cooper-Frye procedure (Eq. (1)) to describe freeze-out in hydrodynamical models is that if the surface element of the freeze-out

surface is spacelike³, particles with certain momenta count as a negative contribution to the distribution: These particles move inwards, they are not emitted at the surface but absorbed⁴. However, in a hybrid model, these negative contributions are only a technical, not a conceptual problem. In an ideal case, the switch from fluid to cascade is done in a spacetime region where both descriptions give (approximately) equal solutions [1]. Thus, in the vicinity of the switching surface the particle distributions are close to thermal, and correspond to the hydrodynamical solution on both sides of the surface. Assuming that the system is dilute enough for the kinetic theory decomposition of the fluid variables in terms of particle distributions to be valid, the particle distributions $f(p, x)$ are known on the surface, and there are particles moving inwards through the surface as described by Cooper-Frye. If this is not the case, the particlization takes place in a region where transport and hydro do not give equal solutions, and the switch from hydro to cascade should take place elsewhere.

Thus as an initial state for the cascade, we have to count the particles passing through the switching surface from hydro to cascade. Their distribution is easily obtained by augmenting the distribution in Eq. (1) by a Θ -function counting particles going outward:

$$E \frac{dN(x)}{dp^3} = d\sigma_\mu p^\mu f(x, p) \Theta(d\sigma_\mu p^\mu). \quad (5)$$

We have to calculate the number of particles coming from hydro to cascade using this distribution, but we must also have a drain term in the cascade: All the particles crossing the particlization surface from cascade to hydro must be removed from the cascade. Otherwise the conservation laws are not obeyed. It is not possible to remove particles from cascade at the rate described by Cooper-Frye procedure, but we can calculate the distribution of particles which were removed from cascade when they entered the fluid dynamical region. This provides a consistency check: At the end of the evolution we can compare whether the phase-space distribution of particles removed from cascade is (approximately) equal to the negative contributions given by Cooper-Frye. If they are, the calculation was consistent, if not, then the switch from hydro to cascade took place in a wrong place, we have to change the switching criterion, and redo the calculation. Of course this argument assumes that such a spacetime region exists where transport and (dissipative) fluid dynamics give equal spacetime evolution. If this is not the case the whole *raison d'être* of hybrid models is questionable, since the switching becomes as arbitrary as the freeze-out in hydrodynamical models.

Unfortunately the treatment described above is technically challenging. First, it is numerically expensive to

³ We use the convention to describe a surface as time- or spacelike according to its normal vector. $d\sigma_\mu d\sigma^\mu > 0$ is timelike, and $d\sigma_\mu d\sigma^\mu < 0$ is spacelike.

⁴ In the context of hydrodynamical models, these negative contributions have been discussed, and possible cures proposed, in Refs. [15, 34, 36, 37, 38].

evaluate the number of particles emitted when the distribution is modified by the Θ -function (Eq. (5)). Second, we are using UrQMD to describe the hadronic transport, and the present version of UrQMD does not allow tracing the propagation of individual particles in such a way that whenever a particle crosses the boundary between cascade and fluid dynamics, it would be removed from cascade. Such a feature would require extensive rewriting of the code, and is therefore postponed to later. Furthermore, we are using ideal hydro to describe the fluid dynamical part, and we do not expect that there exists a region where UrQMD would lead to ideal fluid dynamical behaviour⁵.

Since the correct treatment is at the time of this writing beyond our reach, we have to settle with an approximative solution like in Ref. [9]: First, we ignore all the surface elements where the flow is directed inwards, *i.e.* where $d\sigma_\mu u^\mu < 0$, since the net number of particles passing through such a surface element is negative. There are more particles moving inwards than outwards. Second, on the surface elements where the flow is directed outwards, $d\sigma_\mu u^\mu > 0$, we use the net number of particles passing the surface, $d\sigma_\mu j^\mu$, as the number of particles emitted, but we use the thermal distribution with Θ -function, Eq. (5) as their momentum distribution. This leads to a small violation of conservation laws. The emitted particles either have too large energy, or we generate too few of them, depending on the constraints we impose on the sampling procedure.

There are approaches in the literature where the problem of negative contributions is solved differently. Instead of sampling the phase-space distributions like we do here, in VISHNU [7,40] and in Ref. [13], the momentum distribution of each particle species is calculated by integrating over the particlization surface, Eq. (1), like in the conventional calculation of particle spectra in hydrodynamical models [41,42]. The number of particles of species i per unit rapidity, dN_i/dy , in these boost-invariant distributions is calculated, and the sampling is constrained to produce either $10dN_i/dy$ particles in a wide rapidity interval of $-5 < y < 5$ [41], or dN_i/dy particles in an interval $-0.5 < y < 0.5$ [13]. These yields are not integers, however. In VISHNU the yield, $10dN_i/dy$, is rounded down to the nearest integer [41], whereas in ref. [13] the decimal part is taken as a probability whether to create one additional particle over the rounded down yield [42]. At this stage the sampled particles carry no information of their position. In Ref. [13] there are no rescatterings after particlization, and this lack of information is not a problem, whereas in VISHNU each particle is given a position according to the probability given by the Cooper-Frye distribution, neglecting the part where the distribution would be negative, Eq. 5. Thus this approach reproduces the Cooper-Frye momentum distribution, but it skews the position distribution of the particles reducing the fraction of particles emitted from timelike surface elements. How this affects the final distribution of particles after rescatterings is unknown. Another disadvantage of this approach is that

since it requires evaluating the momentum distributions of all particle species by integrating over the particlization surface, it is slow.

As mentioned in the beginning of this section we want to switch from fluid to cascade in a region where both approaches give similar results, and that there is no physical change in the region where the switch takes place. This means that the solutions to the negative contributions at freeze-out proposed in Refs. [34,36,37] are not applicable in our case. In those approaches a non-thermal freeze-out distribution which contains no particles moving inwards is postulated. But since we assume that the distributions are the same on both sides of the switching surface, such a distribution on the particle side would be a contradiction. Furthermore it is perfectly possible that the hadrons in the cascade scatter back to the spacetime region described by fluid dynamics, and assuming that there are no particles entering that region is an oversimplification.

4 Sampling the distributions

Any hadron cascade requires a particle ensemble with well defined particle species, momenta, and positions as an initial state. To generate such an ensemble we Monte-Carlo sample the particle distributions on the particlization surface. For this purpose we employ two different sampling algorithms. The first one that we call 'allcells' sampling, contains a loop over all hypersurface elements and in each of the elements, *i.e.* cells, the particles are sampled according to the steps explained below. In this case the quantum numbers like energy, net baryon number, net strangeness and electric charge are only conserved on the average over many sampled events. The other algorithm that is dubbed 'mode' sampling introduces a way to conserve all these quantities event-by-event, as we will demonstrate in Section 5.4. The whole sampling algorithm is based on previous work published in [5], but now applied without the assumption of an isochronous transition and with slight improvements.

In general fluctuations in conserved quantum numbers occur in event-by-event studies when only part of the system is described. For example, the spectators are usually not included in the hydrodynamical description of the system. As well fluctuations occur in a rapidity interval which does not contain all the emitted particles. But, once an initial state of the system is defined, and the whole subsequent evolution is considered, the conserved quantum numbers must be conserved. The straightforward 'allcells' sampling does not do it, and therefore we have developed the more complicated 'mode' sampling approach.

The first step in sampling hadrons on the hypersurface is to decide in which cells a particle has been produced. For example, in a central Au+Au collision at the highest RHIC energy there are roughly 10^7 hypersurface elements, but only $\sim 10,000$ particles produced. Evaluating first, if there is a particle produced in a cell, before doing any of the other steps, results in a speed-up of the calculation, which is essential for the application to event-by-event calculations.

⁵ For the difficulties in approaching the ideal fluid limit using transport, see *e.g.* Ref. [39].

The number of particles of each hadron species produced in one cell is calculated according to the following formula (only the surface elements with $u^\mu d\sigma_\mu > 0$ are considered) :

$$N_i = j^\mu d\sigma_\mu = n_i u^\mu d\sigma_\mu, \quad (6)$$

where n_i is the particle density in the local rest frame and i is the index of the particle species. It is important to take into account all 150 particle species and their antiparticles implemented in UrQMD to match the equation of state on the particlization surface. Assuming a Boltzmann distribution the integral over momentum space for the particle number density in the local rest frame can be evaluated analytically and the result is

$$n_i = \frac{4\pi g_i m_i^2 T}{(2\pi)^3} e^{\frac{\mu}{T}} K_2\left(\frac{m_i}{T}\right), \quad (7)$$

where g_i is the degeneracy factor for the respective particle species. All the information about the particle properties is read in directly from the UrQMD tables to avoid any mismatch. The chemical potential includes the baryochemical potential and the strangeness chemical potential in the following way

$$\mu = B \cdot \mu_B + S \cdot \mu_S, \quad (8)$$

where S is the quantum number for strangeness and B is the baryon number. For pions the Bose distribution has to be taken into account because their mass is on the order of the temperature of the system. Expanding the distribution in series and integrating leads to

$$n_\pi = \frac{g_\pi m_\pi^2 T}{(2\pi)^2} \sum_{k=1}^{\infty} \frac{1}{k} K_2\left(\frac{km_\pi}{T}\right), \quad (9)$$

where we stop the summation after 10 summands, when it has sufficiently converged.

By summing up all the contributions from different species the total number of particles in this cell $N = \sum N_i$ is known. As long as $N < 0.01$ one can interpret this number directly as a sampling probability and randomly decide, if a particle is produced or not. If N is larger, one needs to sample a Poisson distribution with N as the mean value to decide the actual number of particles produced in this surface element. It turns out that the cases where 2 or more particles per cell are produced are rare. If there is a particle produced the species can be decided by sampling according to their probabilities N_i/N . Isospin is assigned randomly consistent with the isospin symmetry of a system in chemical equilibrium.

The four momenta of the particles are sampled according to the local Cooper-Frye distribution (only the parts where $f(x, p)p^\mu d\sigma_\mu > 0$ are considered)

$$\frac{dN(x)}{d^3p} = \frac{1}{E} f(x, p) p^\mu d\sigma_\mu, \quad (10)$$

where $f(x, p)$ are the boosted Fermi or Bose distributions corresponding to the respective particle species including again the chemical potentials for baryon number and

strangeness. Finding the maximum of the distribution and then applying the rejection method is crucial since the distribution functions in momentum space are highly peaked and dependent on the masses and thermodynamic parameters. Currently, an approximative maximum of

$$\frac{1}{E} p^\mu d\sigma_\mu f(x, p) \quad (11)$$

is determined by a coarse loop over the three-dimensional momentum space. This approximate maximum is multiplied by 1.2 to make sure it is definitely larger than the function to be sampled.

Then, a momentum vector \mathbf{p} is chosen randomly, and an additional random number between zero and the above mentioned maximum of the distribution is generated. If this random number is smaller than the value of the distribution at this momentum, the momentum is accepted. If not, another momentum and another random number are generated, and the process is repeated until an acceptable momentum is found.

As described in Sec. 3 we neglect negative parts of the distribution functions which slightly alters the resulting rapidity and transverse momentum spectra. It is important to sample the momenta according to the boosted distribution function instead of sampling the equilibrium distribution in the local rest frame and then boost the momentum four-vector back to the computational frame. The second procedure leads to a violation of energy conservation since one does not reproduce the whole tensor $T^{\mu\nu}$ in the computational frame correctly [16].

Imposing strict conservation laws on grand canonical distributions on event-by-event basis is not wholly consistent, and we minimise any bias it creates by the following procedure: To conserve energy, net baryon number, net strangeness and electric charge in all events we do seven subsequent random loops called modes over the hypersurface. During the first mode, cells are randomly chosen and particles are sampled until the total energy is conserved. From this set of particles only the ones containing a \bar{s} quark are kept, and the rest are discarded. In the second mode we produce particles in a similar way, until we've produced as much anti-strangeness as the first mode produced strangeness. We keep the anti-strange particles, and discard the rest. In modes three and four we repeat the same procedure keeping the non-strange baryons and non-strange antibaryons, respectively, but requiring that the net baryon number of these particles is the net baryon number of the system. Modes five and six take care of the conservation of electric charge by keeping the negative and positive non-strange mesons, respectively, and finally mode seven takes care of the energy conservation by sampling neutral non-strange mesons until the energy of the particles corresponds to the energy of the fluid.

5 Results

5.1 Description of the Hybrid Model

The hypersurface finding and sampling algorithms described in Sections 2 and 4 have been implemented in the hybrid

model of Ref. [5]. We show here some preliminary results to demonstrate some general trends and overall behaviour of the improved model. Note that we have not tried to fine-tune any parameters to describe experimental data at this point.

Smooth initial conditions for the hydrodynamic evolution have been generated by averaging over 100 UrQMD events that are run up to the starting time of $t_{\text{start}} = 2.83$ fm for Pb+Pb collisions at $E_{\text{lab}} = 160A$ GeV (SPS) [43] and $t_{\text{start}} = 0.5$ fm for Au+Au collisions at $E_{\text{cm}} = 200A$ GeV [44] (RHIC).

On the constant time surface $t = t_{\text{start}}$ the energy, momentum and net baryon number densities are determined by representing each particle in the UrQMD event with a three-dimensional, longitudinally Lorentz-contracted, Gaussian density distribution of thermalised matter, which has the same energy, momentum and baryon number than the particle it represents. Summing up the distributions representing the particles, we obtain a distribution of matter in thermal equilibrium, which has the same energy, momentum and baryon number than the UrQMD event in question. For the RHIC initial state we consider only particles within the rapidity interval $-2 < y < 2$, whereas we include all particles that have interacted at least once when evaluating the initial state for SPS. The mean value of these distributions from 100 events leads to a smooth profile but still includes finite initial velocities in all three directions [45].

The (3+1)D ideal hydrodynamic evolution is solved in Cartesian coordinates using the SHASTA algorithm [46, 47]. The equation of state is calculated within a chiral model coupled to the Polyakov loop to include the deconfinement transition that reproduces nuclear ground state properties and lattice QCD data at zero net-baryon chemical potential [48]. This equation of state is also applicable at finite net baryon densities, which allows us to calculate heavy ion collisions at SPS energies to explore the beam energy dependence of our findings. In the hadronic phase this equation of state is equivalent to the effective equation of state of UrQMD, and has the same degrees of freedom than UrQMD. The conservation laws are thus automatically fulfilled on particlization surface when we use Cooper-Frye prescription to calculate the particle distributions.

The hypersurface finder 'cornelius' has been implemented in the hydrodynamic code in such a way that the hypersurface for any transition criterion is evaluated while the hydrodynamic evolution is calculated. Then we apply the two sampling algorithms and further calculate resonance decays using UrQMD. To obtain final results that can be compared to experimental data the hadronic transport approach is used in addition to calculate the rescatterings.

5.2 Structure of the Hypersurface

The equations of motion of relativistic hydrodynamics are nothing more than an application of conservation laws for energy, momentum and charge(s). Thus one of the first

Table 1. The conservation of energy (E) and net baryon number (B) in Au+Au collisions at $E_{\text{cm}} = 200A$ GeV. The values in the final state are split into two parts: *pos.* is flow through elements where the energy or baryon flow is directed outwards, $d\sigma_{\mu}T^{\mu 0} > 0$ or $d\sigma_{\mu}n_B u^{\mu} > 0$, respectively, whereas *neg.* is flow through elements where energy or baryon flow is directed inwards, $d\sigma_{\mu}T^{\mu 0} < 0$ or $d\sigma_{\mu}n_B u^{\mu} < 0$, respectively, and thus counts as negative. Note that these are not the negative contributions of Cooper-Frye, see the text. The upper two rows are for central ($b < 3.4$ fm) and the lower two rows for mid-central ($b = 7$ fm) collisions.

	E [GeV]			B		
	total	<i>pos.</i>	<i>neg.</i>	total	<i>pos.</i>	<i>neg.</i>
initial	5431			93.23		
final	5430	5861	-431	92.74	97.74	-5.00
initial	2327			35.84		
final	2336	2455	-119	35.80	37.10	-1.30

Table 2. The conservation of energy (E) and net baryon number (B) in Pb+Pb collisions at $E_{\text{lab}} = 160A$ GeV. The layout is the same as in Table 1.

	E [GeV]			B		
	total	<i>pos.</i>	<i>neg.</i>	total	<i>pos.</i>	<i>neg.</i>
initial	3117			347.6		
final	3120	3208	-88.5	345.9	355.8	-9.9
initial	1528			170.23		
final	1528	1570	-41.5	169.22	174.26	-5.04

checks on the accuracy of the numerical solutions of hydrodynamics is to confirm the validity of the conservation laws.

We show the total energy (E) and net baryon number (B) in collisions at two different centralities at RHIC and SPS in tables 1 and 2, respectively. The initial value is evaluated in the beginning of the hydrodynamical evolution by summing over all fluid cells within the particlization surface. With the switching criterion we use here, $\epsilon = 2\epsilon_0$, where ϵ_0 refers to the nuclear ground state energy density of $146 \text{ MeV}/\text{fm}^3$, this means summing over the cells with $\epsilon > 2\epsilon_0$. Since the final state we are interested in is the isosurface with $\epsilon = 2\epsilon_0$, we evaluate the final state energy and net baryon number as energy and baryon number flows through this surface:

$$E = \int_{\sigma} T^{0\mu} d\sigma_{\mu} \quad \text{and} \quad B = \int_{\sigma} n_B u^{\mu} d\sigma_{\mu}, \quad (12)$$

where the energy momentum tensor has been evaluated as $T^{\mu\nu} = (\epsilon + P)u^{\mu}u^{\nu} - g^{\mu\nu}P$. As seen in the tables both the energy and baryon number are nicely conserved with better than 0.6% accuracy in all cases.

However, a closer look at the properties of the particlization surface reveals that there are surface elements where the flow is directed inwards, $d\sigma_{\mu}u^{\mu} < 0$. As described in Sec. 4, such elements cannot be used as a source for sampled particles, and thus we check how large uncertainty these elements cause to the total energy and baryon number. In tables 1 and 2, the flows through the surface

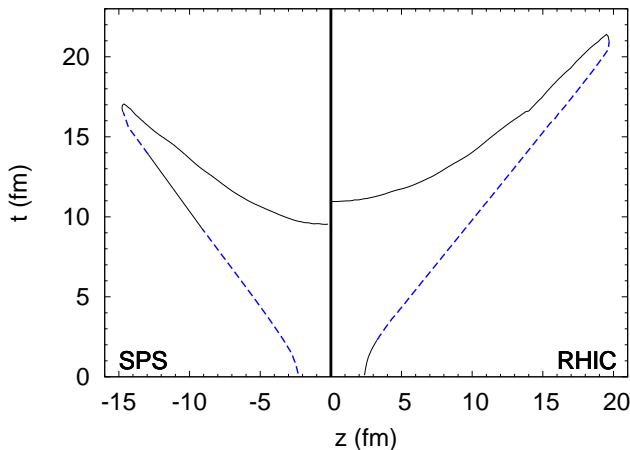


Fig. 11. The position of the $\epsilon = 2\epsilon_0$ isosurface in zt -plane at $x = y = 0$. The left side of the plot (SPS) depicts the surface in central Pb+Pb collisions at $E_{\text{lab}} = 160A$ GeV and the right side (RHIC) in central Au+Au collisions at $E_{\text{cm}} = 200A$ GeV. The dashed lines depict regions where the flow may be directed inwards on some surface elements.

are also separated in two parts: *pos.* depicts the energy and baryon flows through surface elements where $d\sigma_\mu T^{\mu 0} > 0$ for energy and $d\sigma_\mu n_B u^\mu > 0$ for baryon flow, whereas *neg.* is the flow through elements where $d\sigma_\mu T^{\mu 0} < 0$ for energy and $d\sigma_\mu n_B u^\mu < 0$ for baryons. As seen the surface elements where flow is directed inwards cause a 3–8% uncertainty in the total energy, and a 3–5% uncertainty in the total baryon number of the system. Note that because of the pressure term in T^{00} it is possible that we have an element where energy flow is directed inwards but baryon flow outwards, or vice versa.

To understand this phenomenon we located the surface elements with $d\sigma_\mu u^\mu < 0$ and found out that they are almost entirely located at the edges of the system where the fireball expands longitudinally, see Fig. 11, and there are none at midrapidity. Furthermore, the regions depicted by dashed lines in Fig. 11 are not regions where the flow is directed inwards, but they are regions where surface elements with inwards directed flow randomly appear among elements where the flow is directed outwards. These are the regions where the longitudinal pressure gradient is still large, the fluid flow is very large, $v_z \sim 0.9$ – 0.95 , and the isosurface moves outwards with a comparable speed as well. It is known that this is a difficult terrain for SHASTA and for any algorithm to solve accurately [46]. Since the flow velocity is almost aligned with the surface, it does not require a large numerical error to flip an outwards flow to inwards. Thus it is possible that these elements with flow directed inwards are just numerical artefacts. However, it is worth remembering that in event-by-event calculations the initial states are highly irregular, and occasionally flow can be directed inwards for physical reasons.

Since the common feature of the elements with inwards directed flow is the large longitudinal flow velocity, we further characterise the surface by it. We bin the surface elements according to the magnitude of the longitudinal

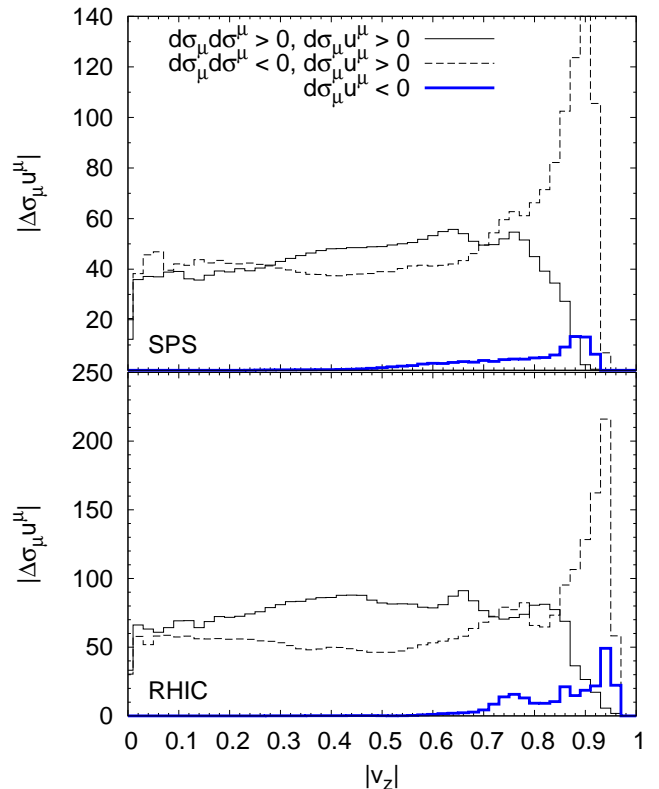


Fig. 12. The magnitude of the fluid flow through different parts of the particlization surface at different longitudinal flow velocities in central Pb+Pb collisions at $E_{\text{lab}} = 160A$ GeV (SPS) and in central Au+Au collisions at $E_{\text{cm}} = 200A$ GeV (RHIC), see the text.

flow velocity $|v_z|$, and integrate over the elements in each bin to obtain the magnitude of fluid flow through surface, $|\Delta\sigma_\mu u^\mu|$, at different velocities $|v_z|$. The results are shown in Fig. 12. The contribution from elements with flow directed inwards is depicted by the thick curve, and as claimed it is concentrated at large velocities. Furthermore it can be seen that the fluid flow inwards is small compared to the fluid flow outwards, which is depicted by the thin solid and dashed histograms in Fig. 12. The 5–8% uncertainties in energy and baryon number listed in tables 1 and 2 are thus concentrated at large longitudinal flow velocities, and can be expected to have only a tiny contribution to observables at midrapidity. The reason why there is a difference between fluid flow $d\sigma_\mu u^\mu$ and energy and baryon number flows, $d\sigma_\mu T^{\mu 0}$ and $d\sigma_\mu j^\mu$, respectively, is that the former has an additional gamma factor and a pressure term, whereas the latter is also sensitive to the baryon chemical potential μ_B which is not uniform on the surface.

5.3 Negative contributions

It is worth remembering that the negative contributions to energy and baryon number discussed above in Sec. 5.2

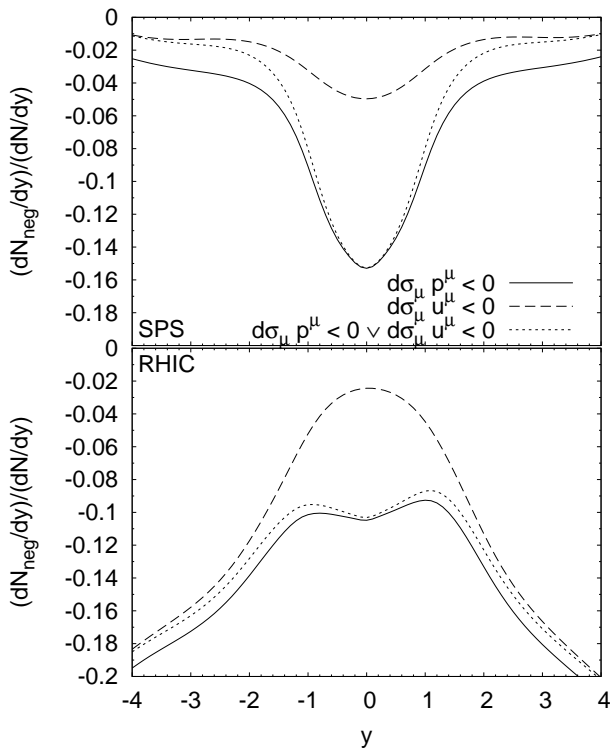


Fig. 13. The ratio of the negative contribution to the total thermal pion rapidity distribution in central Pb+Pb collisions at $E_{\text{lab}} = 160A$ GeV (SPS) and in central Au+Au collisions at $E_{\text{cm}} = 200A$ GeV (RHIC). The curves correspond to different kinds of contributions, see the text.

are not the same thing than the negative contributions of Cooper-Frye discussed in the literature (see Sec. 3). The former are caused by the collective flow being directed inwards, whereas the negative contributions of Cooper-Frye are caused by individual particles moving inwards through the particlization surface. As discussed in Sec. 4, the sampling routine cannot take into account particles moving inwards nor anything emitted on surfaces where flow is directed inwards. Therefore we evaluated these negative contributions to see how much omitting them distorts the spectra.

We evaluated the spectra of thermal pions, kaons and protons on the particlization surface using the conventional Cooper-Frye procedure, Eq. (1), *i.e.* we integrated over the surface to obtain distributions, but we divided the contribution into four parts according to whether the flow was directed in- or outwards ($d\sigma_{\mu}u^{\mu} < 0$ or > 0) and whether the particles with the momentum in question were heading in- or outwards ($d\sigma_{\mu}p^{\mu} < 0$ or > 0). It turned out that in general the negative contributions to pion distribution are largest, so we concentrate on them. Some of the actual spectra are shown in Sec. 5.5 where we compare the sampled distributions to the integrated ones. Here we emphasise the size of the negative contributions by showing their relative contribution to the total spectrum.

In Fig. 13 different negative contributions to the thermal pion rapidity spectrum are shown for collisions at RHIC and SPS. To check how much uncertainty the contribution from elements with flow directed inwards cause, we have calculated the contribution from them (dashed line, $d\sigma_{\mu}u^{\mu} > 0$) even if contribution from them is not negative in the Cooper-Frye sense. It is seen that at midrapidity contribution from them is 2–5%. A modest contribution at midrapidity could be expected, since as shown in Fig. 12, the longitudinal flow velocity on these elements is large. Interestingly the contribution from these elements at large rapidities is very different at RHIC and SPS: The magnitude of the relative contribution decreases with increasing rapidity at SPS, but increases at RHIC. Again a result of different flow and emission patterns shown in Fig. 12.

We may take the surface and flow pattern as granted, and simply evaluate the fraction of inwards moving particles. This is depicted by the solid line, $d\sigma_{\mu}p^{\mu} < 0$, in Fig. 13. At midrapidity the contribution of such a particles is surprisingly large, 10–15% with a larger contribution at SPS than at RHIC. That the negative contribution is larger at SPS was already implied in Fig. 12 where the fluid flow through the particlization surface was divided into a flow through time- and spacelike surfaces. At SPS the relative fraction of the fluid flow passing through spacelike surfaces is larger than at RHIC. Since negative contributions appear only on spacelike surfaces, the flow pattern at SPS provides a possibility for larger negative contributions than at RHIC. Furthermore, if surfaces are similar, the lower the flow velocity, the larger the negative contributions. At SPS the flow velocity is lower than at RHIC, and thus it is rather surprising that the difference in negative contributions is not larger than what is shown in Fig. 13.

Finally, we want to check how large contribution our sampling routine misses. Since it cannot sample the particles going inwards nor particles emitted when the flow is directed inwards, sampling misses both contributions. This is shown as the dotted line in Fig. 13. At midrapidity the missed part is totally dominated by the conventional negative Cooper-Frye contribution. Thus it is safe to say that what comes to sampling particles at midrapidity, the inwards directed flow is not a problem, but the conventional negative contributions of Cooper-Frye can be.

To further study the effect of negative contributions, we show the contributions to p_T distribution of thermal pions at midrapidity, $-1 < y < 1$, in Fig. 14. Again we see that the contribution from the inwards directed flow is smaller than from inwards moving particles. The latter can even reach 40% at low values of transverse momentum! Fortunately the size of the negative contribution decreases rapidly with increasing transverse momentum, and already around 500 MeV they are much more acceptable 8–10%. That the negative contributions are largest at small p_T is understandable since the high p_T particles are mostly emitted in regions where the flow velocity is large and parallel to momentum, whereas the negative contri-

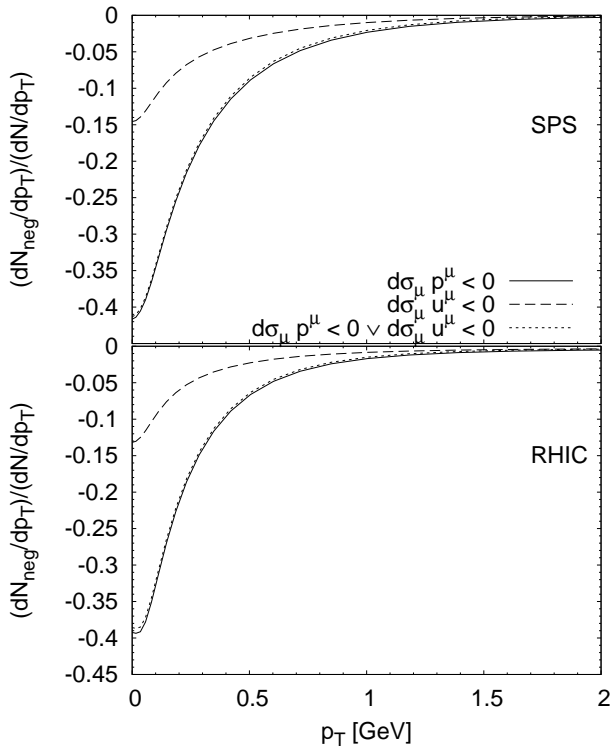


Fig. 14. The ratio of the negative contribution to the total thermal pion p_T -distribution at midrapidity $-1 < y < 1$ in central Pb+Pb collisions at $E_{\text{lab}} = 160A$ GeV (SPS) and in central Au+Au collisions at $E_{\text{cm}} = 200A$ GeV (RHIC). The curves correspond to different kinds of contributions, see the text.

butions arise when the momentum is antiparallel to flow velocity.

We also evaluated the p_T averaged v_2 of thermal pions at particlization in mid-central ($b = 7$ fm) collisions at RHIC and SPS. When v_2 was evaluated in a conventional fashion, we got $v_2 = 0.064$ and 0.066 at RHIC and SPS, respectively. When we removed the negative contributions from the distribution, v_2 at RHIC and SPS decreased to 0.058 and 0.06 , respectively. If we also removed the remaining positive contribution from elements with flow directed inwards, further change on v_2 was on the level of 10^{-4} . This additional uncertainty of 10% should be kept in mind when discussing the elusiveness of the QGP shear viscosity [49].

5.4 Conservation of Quantum Numbers

In Figs. 15 and 16 we show the probability distributions of relevant quantum numbers using the two sampling algorithms described in Section 4. As explained, the 'mode' sampling is constructed to obey conservation laws event-by-event, whereas in the simpler sampling of all hypersurface elements the conserved quantities fluctuate around the values given by the positive contributions to the spectra. Note that these values are not those given in Tables 1 and 2 as energy and baryon number flow through the parts

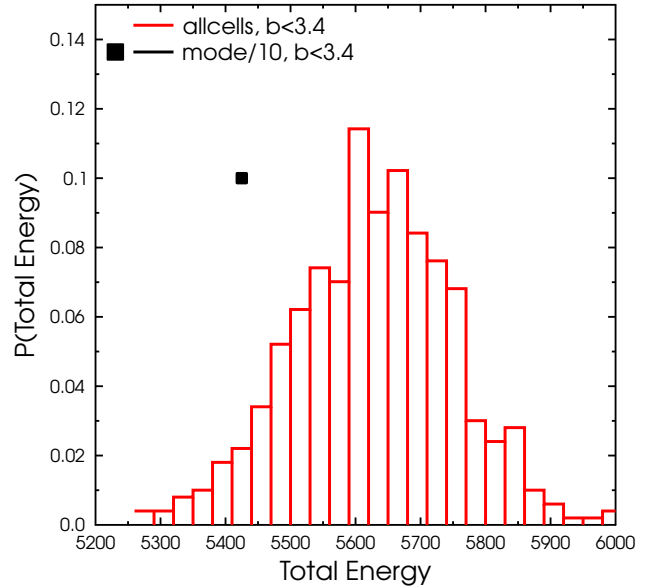


Fig. 15. Probability distribution for the total energy of an event in an ensemble of 500 events created using two different sampling algorithms in central Au+Au collisions at $E_{\text{cm}} = 200A$ GeV.

of surface where flow is directed outwards, but by the distributions of particles coming out through these parts of the surface, Eq. (5), after these distributions have been scaled to yield the same number of particles than the local net flow of particles through the surface element, $d\sigma_\mu n u^\mu$. Therefore, we expect to see a higher mean value in the energy and net baryon number in the allcells sampling compared to the mode setup. One of the reasons to implement the mode sampling was to take into account the distortions caused by different kinds of negative contributions by enforcing the conservation laws⁶.

The probability distributions for the different quantities are rather wide in the allcells sampling, so individual events in the more often applied algorithm can have quantum numbers that are far away from their actual values in that event. In a sense this is reasonable since the equation of state used during the hydrodynamical stage, and the particle distributions sampled at particlization assume a grand-canonical ensemble where conservation laws are obeyed only in average. But if we aim at a description of the collisions on an event-by-event basis, we have a contradiction: In nature conservation laws are obeyed in every single event. Thus it makes sense to require that the conservation laws are strictly obeyed during all stages of the model, and check how much the fluctuations created by the sampling procedure affect the observables.

⁶ Remember that in event-by-event simulations inwards flow can be physical.

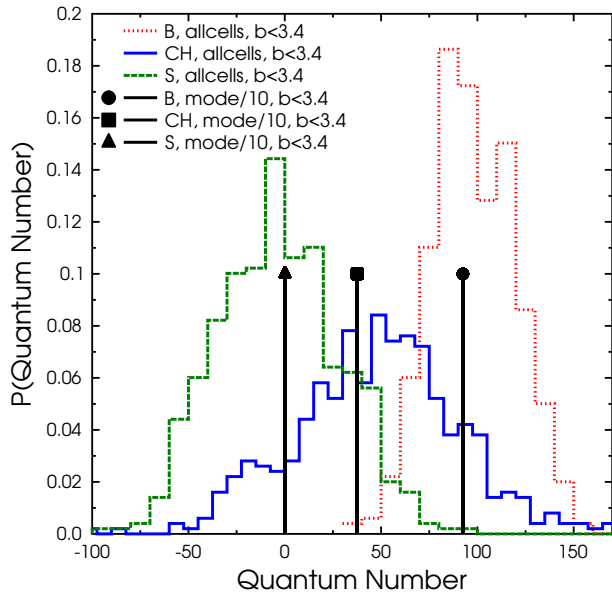


Fig. 16. Probability distribution for the total net baryon number (B), net strangeness (S) and net charge (CH) of an event in an ensemble of 500 events created using two different sampling algorithms in central Au+Au collisions at $E_{cm} = 200A$ GeV.

5.5 Tests of Sampling Algorithm

First of all, we need to check, whether the sampling algorithm reproduces the numbers of particles for each species. In Figs. 17 and 18 the multiplicities of selected particle species are compared to the integrated results. Integration means here summing up N_i as defined in equation 6 for all hypersurface elements where $d\sigma_\mu u^\mu > 0$. All the results in this section are comparisons of thermal yields for individual species only, the resonance contribution has not been included.

We have plotted in Figs. 17 and 18 the relative deviations from the integrated result, $(\# \text{ sampled} - \# \text{ integrated}) / \# \text{ integrated}$, for the two sampling algorithms. The deviations from zero are within the expected statistical fluctuations for 500 events taking into account their individual abundances for the allcells sampling. Overall, in the allcells sampling the particle multiplicities are nicely reproduced at RHIC and SPS energies, whereas the mode sampling leads to slightly less particles at RHIC. This result is expected, since we enforce a lower value for the total energy of the system. The fluctuations of the particle yields around that lower value are again purely statistical. Since at SPS the inwards directed flow is smaller this difference is also smaller and therefore the difference between allcells and mode sampled yields is smaller. As one can see in the rapidity spectra (Figs. 19 and 21), at SPS energies mode sampling produces more particles than allcells sampling.

The next step is to compare the distribution of the particles in momentum space in terms of rapidity and trans-

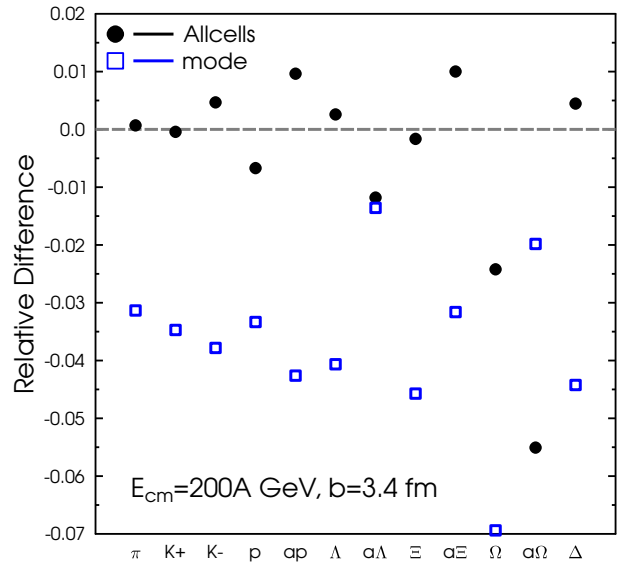


Fig. 17. Relative difference of sampled and integrated particle multiplicities in central Au+Au collisions at $E_{cm} = 200A$ GeV.

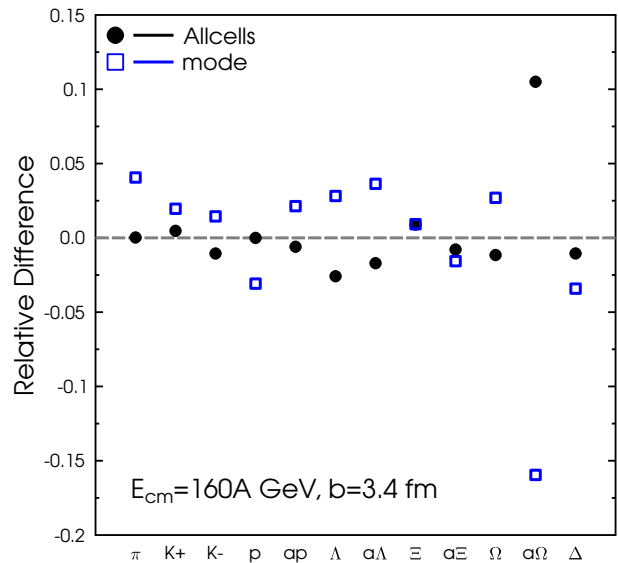


Fig. 18. Relative difference of sampled and integrated particle multiplicities in central Pb+Pb collisions at $E_{lab} = 160A$ GeV.

verse momentum. The different lines in Fig. 19 correspond to the integrated result, which is split up into the different contributions depending on the direction of flow and momentum with respect to the particleization surface as described in the legend, see Sec. 5.3.

For clarity all the contributions are displayed only for pions while for kaons and protons only the full result and

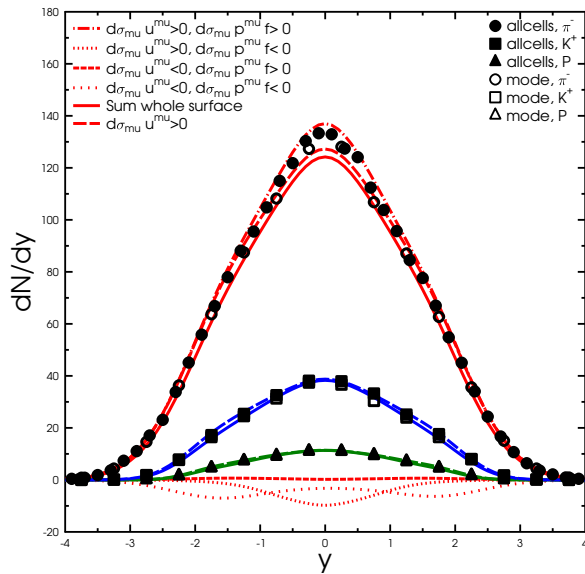


Fig. 19. Comparison of the integrated and sampled rapidity spectra for pions, kaons and protons in central Au+Au collisions at $E_{\text{cm}} = 200A$ GeV.

the result from hypersurface elements with flow directed outwards are shown. The full line corresponds to the full result from the complete hypersurface integration that one ideally wants to reproduce. The dashed line shows the result for the contribution from the cells where the flow is directed outward; these are the cells we take into account when sampling the particle number densities. The momentum sampling on the other hand disregards all the negative parts of the distribution function. This treatment slightly skews the spectrum such that we end up with a result that is in between the dashed and the dot-dashed line for the sampled spectra. It may look surprising that the sampling does not reproduce the yield from outward flowing elements at midrapidity. After all, the sampling procedure has been normalised to reproduce the yield from those elements. The reason for this deviation is that the system in our calculations is not boost invariant. If it were, the edges of the system in longitudinal direction would be infinitely far away, and they would not contribute to midrapidity. But in our non-boost invariant system they are close, and we see the same to happen in longitudinal direction than what is depicted in Fig. 14 for transverse direction: The low momentum, *i.e.* small rapidity, region is depleted because of the negative contributions. The distributions we sample do not contain this depletion, and thus we end up having too many particles at midrapidity. On the other hand, since the sampling procedure reproduces the total yield of particles as shown in Figs. 17 and 18, we must have fewer particles somewhere. A closer look at the spectra reveals that the sampled yield is below the $d\sigma_{\mu}u^{\mu} > 0$ curve at rapidities $1 < |y| < 2.5$, and this deficit is sufficient to cover the excess at midrapidity.

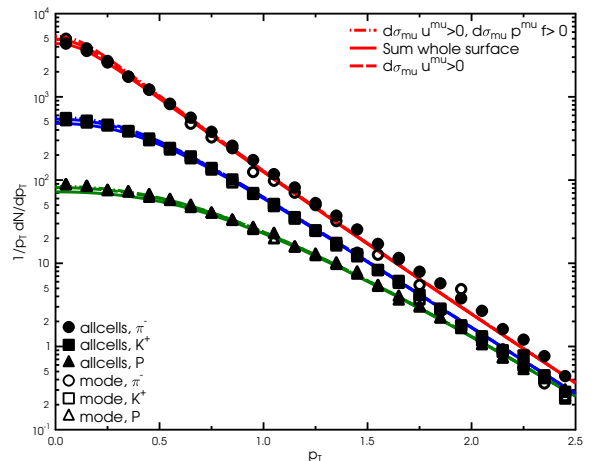


Fig. 20. Comparison of the integrated and sampled transverse momentum spectra for pions, kaons and protons in central Au+Au collisions at $E_{\text{cm}} = 200A$ GeV.

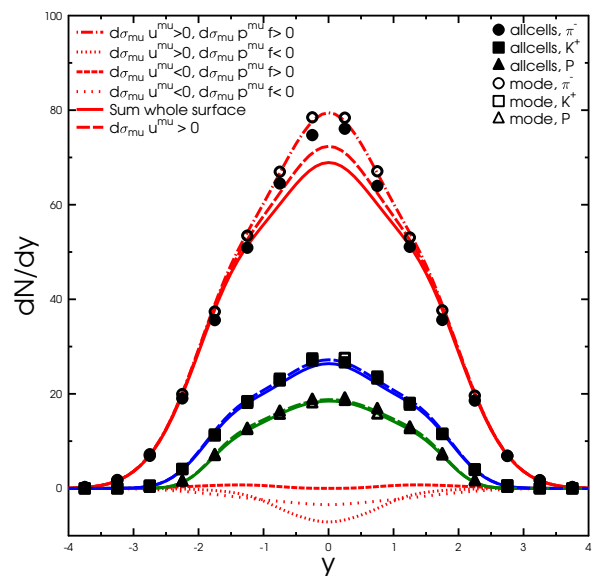


Fig. 21. Comparison of the integrated and sampled rapidity spectra for pions, kaons and protons in central Pb+Pb collisions at $E_{\text{lab}} = 160A$ GeV.

The transverse momentum spectrum is shown in Fig. 20. Due to the logarithmic scale in this case, the differences shown in Fig 14 disappear, and only a small difference between the elements with flow directed outwards and the full result is visible at low transverse momentum. The sampled results are in very good agreement with the integrated results. All possible deviations (apart from statistical noise) are smaller than the size of the symbols.

The comparison of rapidity spectra and transverse momentum spectra at SPS, as shown in Figs. 21 and 22, leads

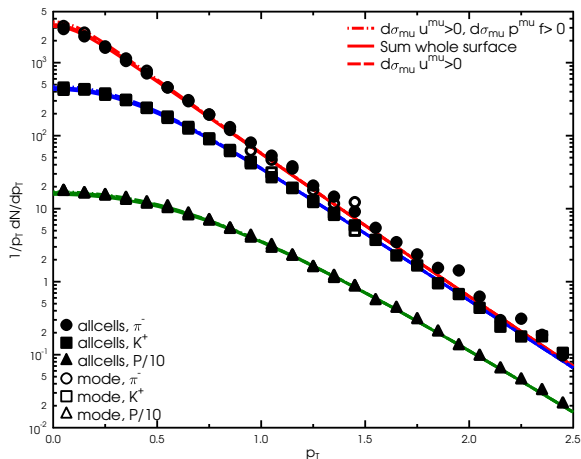


Fig. 22. Comparison of the integrated and sampled transverse momentum spectra for pions, kaons and protons in central Pb+Pb collisions at $E_{\text{lab}} = 160A$ GeV.

to very similar results. The only difference is that in the mode sampling there are more pions produced than in the allcells sampling as mentioned above. The reason for this has to be investigated further in the future.

Overall, the sampling algorithms reproduce the particle yields and spectra very well within the expected deviations from the assumptions that are made in the different algorithms. The negative contributions are also smaller than 5 % in the regions where most of the particles are emitted and affect heavier particles less than lighter ones.

5.6 Effects of Rescattering

In this Section we present selected results for multiplicities, spectra and elliptic flow to demonstrate the effect of the hadronic rescattering and the switching criterion. All the results are calculated using the hybrid approach described in Sec. 5.1 with mode sampling enforcing exact conservation laws. To obtain the results directly at the switching hypersurface we run UrQMD for 0.1 fm and use it only to calculate the resonance decays ('Hydro'). The second option is to run UrQMD for 200 fm and include all the rescattering dynamics in the hadron transport approach ('After').

In Fig. 23 the yields of pions, kaons, protons and Lambdas are shown in central heavy ion collisions at the highest RHIC energy. The final results using allcells sampling are within 3% to the ones shown here (see Fig. 17). Therefore, we decided to restrict the number of shown results to mode sampling only. The switching criteria that we have chosen correspond to the following temperatures $3\epsilon_0 \approx 163$ MeV, $2\epsilon_0 \approx 154$ MeV and $1.5\epsilon_0 \approx 149$ MeV and are in the ballpark of switching criteria that are commonly used in other hybrid approaches [1, 2, 3, 4, 5, 6, 7, 8, 9]. The energy density ϵ_0 refers to the nuclear ground state energy density 146 MeV/fm³. The switching criterion needs to be adjusted together with equation of state and parameters defining the

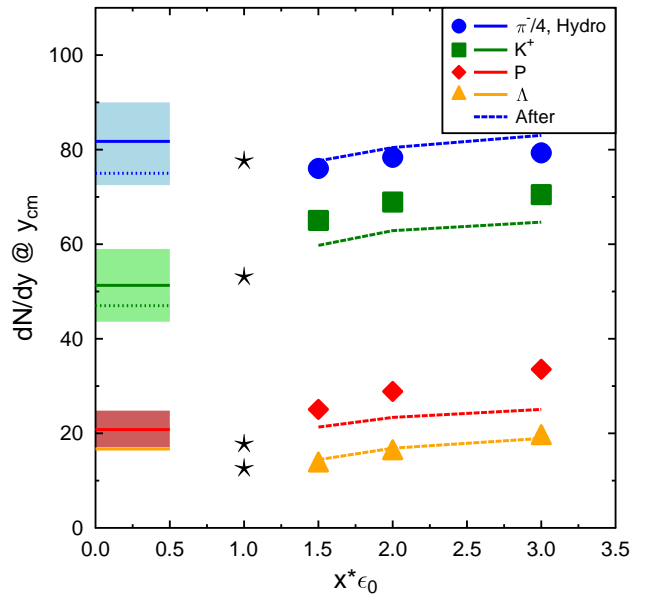


Fig. 23. Yields at midrapidity ($|y| < 0.5$) as a function of switching criterion in multiples of ϵ_0 for four different particle species (π^- , K^+ , P , Λ) in central ($b < 3.4$ fm) Au+Au collisions at $\sqrt{s_{\text{NN}}} = 200$ GeV. The symbols indicate the result with resonance decays ('Hydro') and the lines show the result after rescattering ('After'). The black stars show the result from the previously used 'gradual' transition. The bands on the left indicate data by the STAR and BRAHMS collaborations [50, 51, 52, 53].

initial conditions to achieve a good agreement with experimental data. In this analysis we concentrate on presenting general features of the results and have not searched for the best agreement with the measurements yet.

The yields are slightly higher for higher switching energy densities, because in equilibrium at this temperature range, higher temperatures lead to higher yields. The deviations from equilibrium caused by the sampling procedure are not large enough to break this rule. The rescattering leads to a reduction of the kaon and proton yield, whereas pions and Lambdas are not so much affected. The kaon and proton yields are also higher in the iso-energy density transition scenario than in the previously employed gradual transition, where full transverse slices are sampled on an isochronous surface, when the whole slice has diluted below $5\epsilon_0$. Apart from the fact that the kaon yield is higher than the experimental data our results are in reasonable agreement with the data.

The mean transverse momentum as a measure of the radial flow development is shown in Fig. 24. In this case the dependence on the switching criterion is opposite to the one of the yields. There are two reasons for this behaviour: The first is that for lower switching energy densities the system stays longer in the hydrodynamic evolution and the particles gain more transverse flow. The second argument is that the total energy needs to be conserved

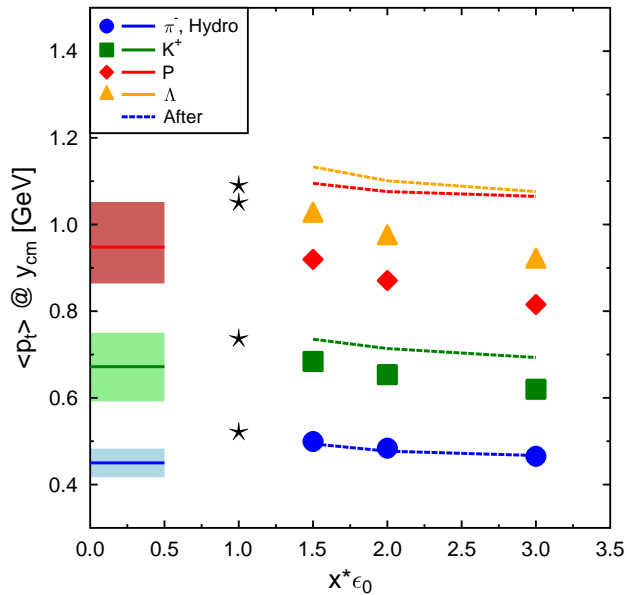


Fig. 24. Mean transverse momentum at midrapidity ($|y| < 0.5$) as a function of switching criterion in multiples of ϵ_0 for four different particle species (π^- , K^+ , P , Λ) in central ($b < 3.4$ fm) Au+Au collisions at $\sqrt{s_{NN}} = 200$ GeV. The symbols indicate the result with resonance decays ('Hydro') and the lines show the result after rescattering ('After'). The black stars show the result from the previously used 'gradual' transition. The bands on the left indicate data by the PHENIX collaboration [54].

and if there are more particles produced, there is less energy remaining to give them kinetic energy in terms of transverse flow at the switching transition. Depending on their hadronic cross-sections and their mass the particles get pushed a lot (e.g. protons) or almost not at all (pions) during the hadronic rescattering stage.

The transverse mass spectra at RHIC and SPS (shown in Figs. 25 and 26 respectively) confirm this behaviour. The pion spectra are almost identical before and after the hadronic cascade, but the kaon and proton spectra begin to resemble the experimental data only after the rescattering. The comparison to the previously imposed gradual transition shows that a true iso-energy density switching criterion improves the slope of the spectra at high transverse masses drastically. This can be easily understood, since in the gradual transition scenario the full slice needs to reach the energy density criterion which delays the switching to hadron cascade for the edges in the transverse direction. The edges gain very large transverse flow velocity, which makes the distributions flatter, and even if the edges get very cold, the yield of heavy particles does not drop so much that the effect of large flow velocity would be negated. What comes to the p_T -distributions, the hybrid model based on ideal hydrodynamics works better at high RHIC energies than at high SPS energies. This indicates

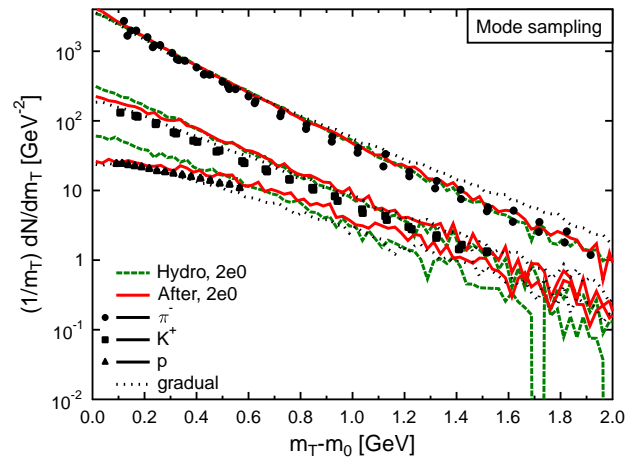


Fig. 25. Transverse mass spectra at midrapidity ($|y| < 0.5$) for pions, kaons and protons in central ($b < 3.4$ fm) Au+Au collisions at $\sqrt{s_{NN}} = 200$ GeV. The dashed lines indicate the result with resonance decays ('Hydro') and the full lines show the result after rescattering ('After'). The black dotted line represents the result from the previously used 'gradual' transition. The symbols indicate experimental data by the STAR, PHENIX and BRAHMS collaborations [52, 55, 54, 56]. The proton data by STAR has been multiplied by 0.6 to correct for the feed-down from Lambdas.

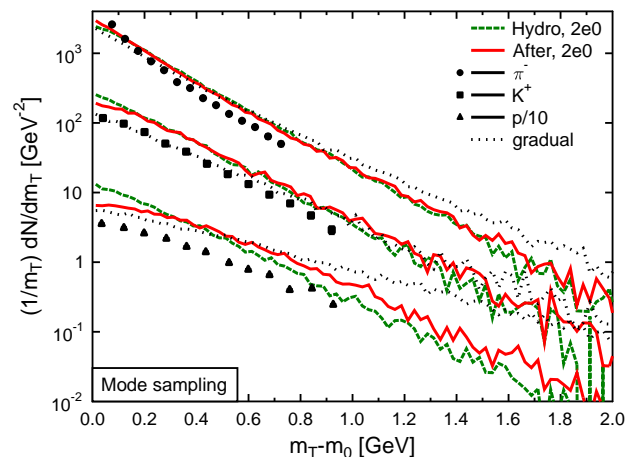


Fig. 26. Transverse mass spectra at midrapidity ($|y| < 0.5$) for pions, kaons and protons in central ($b < 3.4$ fm) Pb+Pb collisions at $E_{lab} = 160A$ GeV. The dashed lines indicate the result with resonance decays ('Hydro') and the full lines show the result after rescattering ('After'). The black dotted line represents the result from the previously used 'gradual' transition. The symbols indicate experimental data by the NA49 collaboration [57, 58].

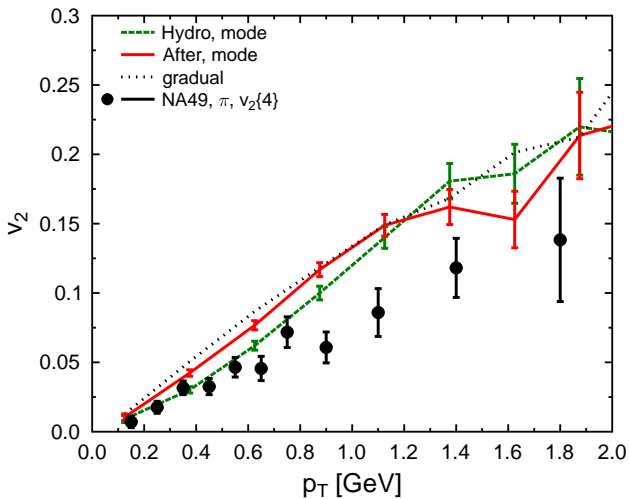


Fig. 27. Elliptic flow of pions as a function of transverse momentum at midrapidity ($|y| < 0.5$) in mid-central ($b = 7$ fm) Pb+Pb collisions at $E_{\text{lab}} = 160A$ GeV. The dashed lines indicate the result with resonance decays ('Hydro') and the full lines show the result after rescattering ('After'). The black dotted line represents the result from the previously used 'gradual' transition. The symbols indicate experimental data by the NA49 collaboration [59].

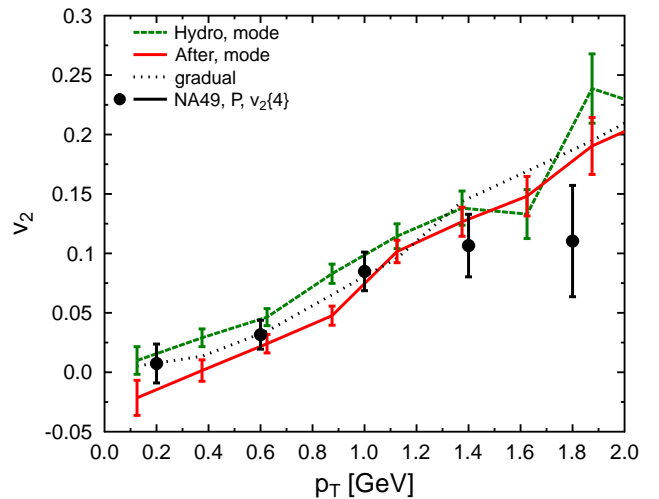


Fig. 28. Elliptic flow of protons as a function of transverse momentum at midrapidity ($|y| < 0.5$) in mid-central ($b = 7$ fm) Pb+Pb collisions at $E_{\text{lab}} = 160A$ GeV. The dashed lines indicate the result with resonance decays ('Hydro') and the full lines show the result after rescattering ('After'). The black dotted line represents the result from the previously used 'gradual' transition. The symbols indicate experimental data by the NA49 collaboration [59].

that the non-equilibrium dynamics gains importance at lower beam energies.

In Figs. 27 and 28 elliptic flow as a function of transverse momentum is shown for pions and protons at high SPS energy. Quite surprisingly the p_T -differential elliptic flow is quite insensitive to the switching criterion. It is known that in ideal fluid hydrodynamics pion $v_2(p_T)$ is quite insensitive to the freeze-out temperature [35]. We presume that the same holds also when one uses the gradual criterion instead of constant temperature/density for particlization, and thus the elliptic flow of pions at particlization is very similar in both cases, and evolves similarly during the cascade. Thus the final $v_2(p_T)$ is similar as well. The proton $v_2(p_T)$ shows more sensitivity than pion $v_2(p_T)$, but the difference is at low p_T , not at high p_T which is influenced by the different evolution of the edges as explained when discussing the p_T spectra. On the other hand, the lower proton v_2 at low p_T is in line with the ideal fluid expectations where lower freeze-out temperature leads to lower proton $v_2(p_T)$ at low p_T . Thus the low p_T range of protons is mostly influenced by the center of the system which evolves hydrodynamically much longer when one uses isodensity switching than when one uses gradual switching. When the hadronic cascade rescattering is taken into account, the proton flow at low transverse momenta seems to even turn negative as recently observed by the CERES collaboration [60].

6 Conclusions

In this paper we have discussed a crucial part of hybrid models in detail: How to switch from hydrodynamical de-

scription to cascade. We have described an algorithm to find an isovalue surface where the transition takes place, the unavoidable negative contributions of Cooper-Frye procedure on such a surface, and how to make the sampling algorithm, which creates the initial state for the cascade, to work on an arbitrary surface and deal with the negative contributions. We have seen that in realistic calculations the negative contributions are not a large problem, but they create an uncertainty of their own which should be kept in mind when one draws conclusions from the results of the present hybrid or hydrodynamical models. In the long run we hope to develop a model where these negative contributions are properly treated, and not just ignored.

We think that the machinery we have described is particularly suitable for a proper event-by-event analysis of heavy-ion collisions. In event-by-event calculations the initial state of hydrodynamics varies wildly from event to event, and thus one may expect the particlization surface to have a very complicated structure. This poses no problem for the algorithm described here since it can create consistent surfaces without holes nor double counting for any configuration. One of the reasons for studying heavy-ion collisions event-by-event are fluctuations. In those studies it is important to distinguish at which stage of the evolution fluctuations are created and how. The sampling algorithm we described provides an important check by allowing strict conservation of energy and charges thus guaranteeing that their fluctuations are not caused by the sampling procedure.

All this machinery is not limited to switching from ideal fluid to cascade, but it can be applied at the interface of viscous hydrodynamics and cascade as well. All

one needs to do is to modify the particle distributions at particlization accordingly.

However, we presented here preliminary results only without attempting to describe the data well. The next step is to identify the main parameters of the hybrid calculation and perform a multi-parameter analysis compared to bulk observables at RHIC using a sophisticated statistical emulator to limit CPU time. Once a good switching criterion has been identified, the beam energy dependence can be explored. In this context, the framework presented here can easily be even more generalised to other switching criteria based on net baryon density, temperature or combinations of thermodynamic quantities.

Acknowledgements:

We are greatly indebted to Bernd Schlei for many informative discussions about surface finding and related algorithms. We thank Tetsufumi Hirano, Huichao Song and Hannu Holopainen for describing their sampling routines in detail. The work of P.H. is supported by BMBF under contract no. 06FY9092 and the work of H.P. by U.S. Department of Energy grant DE-FG02-05ER41367. We are grateful to the Open Science Grid for providing computing resources. H.P. thanks J. W. Goethe Universität and HICforFAIR for hospitality during several stages of this work.

References

1. S. A. Bass and A. Dumitru, Phys. Rev. C **61** (2000) 064909 [nucl-th/0001033].
2. D. Teaney, J. Lauret and E. V. Shuryak, nucl-th/0110037.
3. T. Hirano, U. W. Heinz, D. Kharzeev, R. Lacey and Y. Nara, Phys. Lett. B **636** (2006) 299 [nucl-th/0511046].
4. C. Nonaka and S. A. Bass, Phys. Rev. C **75** (2007) 014902 [nucl-th/0607018].
5. H. Petersen, J. Steinheimer, G. Burau, M. Bleicher and H. Stoecker, Phys. Rev. C **78** (2008) 044901 [arXiv:0806.1695 [nucl-th]].
6. K. Werner, I. Karpenko, T. Pierog, M. Bleicher and K. Mikhailov, Phys. Rev. C **82** (2010) 044904 [arXiv:1004.0805 [nucl-th]].
7. H. Song, S. A. Bass, U. Heinz, T. Hirano and C. Shen, Phys. Rev. Lett. **106** (2011) 192301 [arXiv:1011.2783 [nucl-th]].
8. I. A. Karpenko, Y. M. Sinyukov and K. Werner, arXiv:1204.5351 [nucl-th].
9. T. Hirano, P. Huovinen, K. Murase and Y. Nara, arXiv:1204.5814 [nucl-th].
10. H. Sorge, Phys. Rev. C **52** (1995) 3291 [nucl-th/9509007].
11. S. A. Bass *et al.*, Prog. Part. Nucl. Phys. **41** (1998) 255 [nucl-th/9803035]; M. Bleicher *et al.*, J. Phys. G G **25** (1999) 1859 [hep-ph/9909407].
12. Y. Nara, N. Otuka, A. Ohnishi, K. Niita and S. Chiba, Phys. Rev. C **61** (2000) 024901 [nucl-th/9904059]; M. Isse, A. Ohnishi, N. Otuka, P. K. Sahu and Y. Nara, Phys. Rev. C **72** (2005), 064908. [arXiv:nucl-th/0502058].
13. H. Holopainen, H. Niemi and K. J. Eskola, Phys. Rev. C **83** (2011) 034901 [arXiv:1007.0368 [hep-ph]].
14. H. Petersen, G.-Y. Qin, S. A. Bass and B. Muller, Phys. Rev. C **82**, 041901 (2010) [arXiv:1008.0625 [nucl-th]].
15. D. H. Rischke, In *Cape Town 1998, Hadrons in dense matter and hadrosynthesis* 21-70 [nucl-th/9809044].
16. F. Cooper and G. Frye, Phys. Rev. D **10** (1974) 186.
17. C. M. Hung and E. V. Shuryak, Phys. Rev. C **57** (1998) 1891 [hep-ph/9709264].
18. C. W. Misner, K. S. Thorne, and J. A. Wheeler, *Gravitation* (Freeman, San Francisco, 1973), Chap. 5.
19. J. C. Roberts and S. Hill, Proc. SPIE **3643** (1999) 170, <http://dx.doi.org/10.1117/12.342833>
20. W. E. Lorenson and H. E. Cline, SIGGRAPH Computer Graphics **21** (1987) 163, <http://dx.doi.org/10.1145/37402.37422>
21. R. Venugopalan, M. Prakash, M. Kataja and P. V. Ruuskanen, Nucl. Phys. A **566** (1994) 473C; J. Sollfrank, P. Huovinen, M. Kataja, P. V. Ruuskanen, M. Prakash and R. Venugopalan, Phys. Rev. C **55** (1997) 392 [nucl-th/9607029].
22. P. F. Kolb, J. Sollfrank and U. W. Heinz, Phys. Rev. C **62** (2000) 054909 [hep-ph/0006129]; P. F. Kolb and R. Rapp, Phys. Rev. C **67** (2003) 044903 [hep-ph/0210222]; P. F. Kolb and U. W. Heinz, In *Hwa, R.C. (ed.) et al.: Quark gluon plasma* 634-714 [nucl-th/0305084]; AZHYDRO is available at <http://www.physics.ohio-state.edu/~froderma/>
23. B. Schenke, S. Jeon and C. Gale, Phys. Rev. C **82** (2010) 014903 [arXiv:1004.1408 [hep-ph]].
24. M. J. Düurst, SIGGRAPH Computer Graphics **22** (1988) 72.
25. E. V. Chernyaev, Technical Report CN/95-17, 1995, unpublished, <http://citeseerx.ist.psu.edu/viewdoc/summary?doi=10.1.1.56.7139>
26. G. Wyvill, C. McPheeters and B. Wyvill, The Visual Computer **2** (1986) 227, <http://dx.doi.org/10.1007/BF01900346> or www.cpsc.ucalgary.ca/~blob/papers/softobjects.pdf
27. J.P. Boris and D.L. Book, J. Comp. Phys. **11** (1973) 38; D.L. Book, J.P. Boris and K. Hain, J. Comp. Phys. **18** (1975) 248; J.P. Boris and D.L. Book, J. Comp. Phys. **20** (1976) 397.
28. J. Bloomenthal, *Graphics Gems IV*, edited by P. S. Heckbert (Academic Press, 1994), <http://www.unchainedgeometry.com/jbloom/papers/polygonizer.pdf>
29. B. Schlei, private communication (2012).
30. B. R. Schlei, Computers & Graphics **36** (2012) 111 arXiv:1011.1787 [cs.CG]
31. J.-P. Thirion and A. Gourdon, INRIA Research Report RR-1672, 1992, unpublished, <http://hal.inria.fr/inria-00074885/en/>
32. M. Fidrich, INRIA Research Report RR-2833, 1996, unpublished, <http://hal.inria.fr/inria-00073858/en/>
33. L. Pang, Q. Wang and X.-N. Wang, arXiv:1205.5019 [nucl-th].
34. Y. Cheng, L. P. Csernai, V. K. Magas, B. R. Schlei and D. Strottman, Phys. Rev. C **81** (2010) 064910 [arXiv:1006.5820 [nucl-th]].
35. P. F. Kolb, P. Huovinen, U. W. Heinz and H. Heiselberg, Phys. Lett. B **500** (2001) 232 [hep-ph/0012137]; P. Huovinen, P. F. Kolb, U. W. Heinz, P. V. Ruuskanen and S. A. Voloshin, Phys. Lett. B **503** (2001) 58 [hep-ph/0101136].
36. K.A. Bugaev, Nucl. Phys. A **606** (1996) 559 ; K.A. Bugaev and M.I. Gorenstein, nucl-th/9903072; K. A. Bugaev, M. I. Gorenstein and W. Greiner, J. Phys. G G **25** (1999) 2147 [nucl-th/9906088].

37. C. Anderlik, Z.I. Lazar, V.K. Magas, L.P. Csernai, H. Stöcker, and W. Greiner, Phys. Rev. **C59** (1999) 388; C. Anderlik, L.P. Csernai, F. Grassi, Y. Hama, T. Kodama, and Z.I. Lazar, Phys. Rev. **C59** (1999) 3309; V.K. Magas *et al.*, Heavy Ion Phys. **9** (1999) 193; K. Tamosiunas and L. P. Csernai, Eur. Phys. J. A **20** (2004) 269 [hep-ph/0403179].
38. S. Bernard, J. A. Maruhn, W. Greiner and D. H. Rischke, Nucl. Phys. A **605** (1996) 566 [nucl-th/9602011].
39. D. Molnar and P. Huovinen, Phys. Rev. Lett. **94** (2005) 012302 [nucl-th/0404065].
40. H. Song, S. A. Bass and U. Heinz, Phys. Rev. C **83** (2011) 024912 [arXiv:1012.0555 [nucl-th]].
41. H. Song, private communication (2011).
42. H. Holopainen, private communication (2011).
43. H. Petersen and M. Bleicher, Phys. Rev. C **81** (2010) 044906 [arXiv:1002.1003 [nucl-th]].
44. H. Petersen, C. Coleman-Smith, S. A. Bass and R. Wolpert, J. Phys. G G **38** (2011) 045102 [arXiv:1012.4629 [nucl-th]].
45. H. Petersen, J. Steinheimer, G. Burau and M. Bleicher, Eur. Phys. J. C **62** (2009) 31.
46. D. H. Rischke, S. Bernard and J. A. Maruhn, Nucl. Phys. A **595** (1995) 346 [nucl-th/9504018].
47. D. H. Rischke, Y. Pursun and J. A. Maruhn, Nucl. Phys. A **595** (1995) 383 [Erratum-ibid. A **596** (1996) 717] [nucl-th/9504021].
48. J. Steinheimer, S. Schramm and H. Stöcker, J. Phys. G G **38** (2011) 035001 [arXiv:1009.5239 [hep-ph]].
49. C. Shen, S. A. Bass, T. Hirano, P. Huovinen, Z. Qiu, H. Song and U. Heinz, J. Phys. G G **38** (2011) 124045 [arXiv:1106.6350 [nucl-th]].
50. D. Ouerdane [BRAHMS Collaboration], Nucl. Phys. A **715** (2003) 478 [arXiv:nucl-ex/0212001].
51. J. H. Lee *et al.* [BRAHMS Collaboration], J. Phys. G **30** (2004) S85.
52. J. Adams *et al.* [STAR Collaboration], Phys. Rev. Lett. **92** (2004) 112301 [arXiv:nucl-ex/0310004].
53. J. Adams *et al.* [STAR Collaboration], Phys. Rev. Lett. **98** (2007) 062301 [arXiv:nucl-ex/0606014].
54. S. S. Adler *et al.* [PHENIX Collaboration], Phys. Rev. C **69** (2004) 034909 [arXiv:nucl-ex/0307022].
55. I. Arsene *et al.* [BRAHMS Collaboration], Phys. Rev. C **72** (2005) 014908 [arXiv:nucl-ex/0503010].
56. J. Adams *et al.* [STAR Collaborations and STAR-RICH Collaborations], arXiv:nucl-ex/0601042.
57. S. V. Afanasiev *et al.* [NA49 Collaboration], Phys. Rev. C **66** (2002) 054902 [arXiv:nucl-ex/0205002].
58. C. Alt *et al.* [NA49 Collaboration], Phys. Rev. C **73** (2006) 044910.
59. C. Alt *et al.* [NA49 Collaboration], Phys. Rev. C **68** (2003) 034903 [arXiv:nucl-ex/0303001].
60. D. Adamova *et al.* [CERES Collaboration], arXiv:1205.3692 [nucl-ex].